HHS Public Access

Author manuscript

Nat Biotechnol. Author manuscript; available in PMC 2018 January 17.

Published in final edited form as:

Nat Biotechnol. 2017 August ; 35(8): 757–764. doi:10.1038/nbt.3892.

Nanoscale imaging of clinical specimens using pathology-optimized expansion microscopy

Yongxin Zhao[+,1], **Octavian Bucur**[+,2,3,4,5], **Humayun Irshad**[2,3,5], **Fei Chen**[1,6,7], **Astrid Weins**[8,9], **Andreea L. Stancu**[2,5], **Eun-Young Oh**[2], **Marcello DiStasio**[2], **Vanda Torous**[2], **Benjamin Glass**[2], **Isaac E. Stillman**[2], **Stuart J. Schnitt**[2], **Andrew H. Beck**[2,3,5,*], and **Edward S. Boyden**[1,6,7,10,*]

[1]MIT Media Lab, Massachusetts Institute of Technology, Cambridge, MA, USA

[2]Department of Pathology and Cancer Research Institute, Beth Israel Deaconess Medical Center, Harvard Medical School, Boston, MA, USA

[3]Ludwig Center at Harvard Medical School, Boston, MA, USA

[4]Institute of Biochemistry of the Romanian Academy, Bucharest, Romania

[5]Broad Institute of MIT and Harvard, Cambridge, MA, USA

[6]Department of Biological Engineering, Massachusetts Institute of Technology, Cambridge, MA, USA

[7]McGovern Institute, Massachusetts Institute of Technology, Cambridge, MA, USA

[8]Department of Pathology, Brigham and Women's Hospital, Harvard Medical School, Boston, MA, USA

[9]Department of Medicine, Renal Division, Brigham and Women's Hospital, Harvard Medical School, Boston, MA, USA

[10]Department of Brain and Cognitive Sciences, Massachusetts Institute of Technology, Cambridge, MA, USA

Abstract

[*]correspondence to abeck2@bidmc.harvard.edu (pathological aspects) and esb@media.mit.edu (technical aspects).
[+]made equal contributions.

AUTHOR CONTRIBUTIONS

Y.Z., O.B., A.H.B. and E.S.B. all contributed key ideas, designed experiments and analyzed data. F.C. and Y.Z. performed SR-SIM experiments on tissues. Y.Z. and O.B. designed and acquired ExPath data for all tissues. H.I., O.B. and Y.Z. analyzed ExPath data for breast benign neoplasia experiments. H.I. developed the computational image analysis framework for the breast benign neoplasia analysis. A.L.S. performed the expert annotation (ground truth) for the image analysis framework. E.Y.O., S.J.S. and B.G. performed the selection and annotation of the breast lesions. A.W., M.D., V.T. and I.E.S. participated in the single blinded test for the ExPath kidney experiment. All authors contributed to the writing of the manuscript. A.H.B. and E.S.B. supervised the project.

COMPETING FINANCIAL INTERESTS

Y.Z., O.B., H.I., A.H.B. and E.S.B. have filed for patent protection on a subset of the technologies here described (U.S. Provisional Application No. 62/299,754). E.S.B. has helped co-found a company to help disseminate expansion microscopy to the community. A.H.B. has helped co-found a company to develop artificial intelligence technology for pathology.

Expansion microscopy (ExM), a method for improving the resolution of light microscopy by physically expanding the specimen, has not been applied to clinical tissue samples. Here we report a clinically optimized form of ExM that supports nanoscale imaging of human tissue specimens that have been fixed with formalin, embedded in paraffin, stained with hematoxylin and eosin (H&E), and/or fresh frozen. The method, which we call expansion pathology (ExPath), converts clinical samples into an ExM-compatible state, then applies an ExM protocol with protein anchoring and mechanical homogenization steps optimized for clinical samples. ExPath enables ~70 nm resolution imaging of diverse biomolecules in intact tissues using conventional diffraction-limited microscopes, and standard antibody and fluorescent DNA in situ hybridization reagents. We use ExPath for optical diagnosis of kidney minimal-change disease, which previously required electron microscopy (EM), and demonstrate high-fidelity computational discrimination between early breast neoplastic lesions that to date have challenged human judgment. ExPath may enable the routine use of nanoscale imaging in pathology and clinical research.

The examination of cellular structures and molecular composition using diffraction-limited microscopy has long been used to diagnose or investigate the pathogenesis of a wide variety of pre-disease and disease states. Biomolecules themselves, however, are nanoscale in dimension and configured with nanoscale precision throughout cells and tissues. In basic science, this organization has begun to be explored using pioneering super-resolution microscopy methods[1–4], as well as EM[5–7], but such strategies require complex hardware, can present a steep learning curve, and are difficult to apply to large-scale human tissues. Accordingly, super-resolution imaging and nanoscopy have not found routine utility in clinical practice, and are rarely applied to clinical samples, even in a research context

Recently, we developed a strategy for imaging large-scale cell and tissue samples by physically, rather than optically, magnifying them[8]. In this strategy, which we call expansion microscopy (ExM), we isotropically expand tissues by embedding them in a dense swellable polymer (e.g., a mesh of sodium polyacrylate synthesized evenly throughout a tissue), which binds key biomolecules or fluorescent labels to the polymer network. Samples are then mechanically homogenized and swelled, so that they can be imaged with nanoscale (e.g., ~70 nm) resolution on conventional diffraction-limited microscopes. Although the original version of ExM required synthesis of a linker to couple fluorescent labels to the polymer, we recently developed a version of ExM, protein retention ExM (proExM), which uses a commercially available anchoring molecule to tie proteins – such as fluorophore-bearing antibodies – directly to the swellable polymer[9].

Here, we report a clinically optimized form of proExM, which we call expansion pathology (ExPath), that is capable of processing most types of clinical samples currently used in pathology – including formalin-fixed paraffin-embedded (FFPE), hematoxylin and eosin (H&E)-stained and fresh frozen human tissue specimens on glass slides. We explore the ability of ExPath to enable nanoscale imaging on a wide variety of tissue samples of importance for pathology. We show in a small-scale study that diseases previously requiring EM for diagnosis, such as kidney minimal change disease[10], can now be directly and accurately diagnosed with ExPath and conventional diffraction-limited light microscopy. As another example, we used ExPath to analyze nuclear atypia of early breast lesions that to

date have challenged human judgment[11], and show that ExPath facilitates computational pathology differentiation of hard-to-diagnose subtypes of these lesions. We anticipate that ExPath will broadly find utility in enabling probing of nanoscale features at the genomic, protein, and cell-morphology levels, enhancing the diagnostic power available to pathologists without investment in novel hardware. We also expect the method will be useful for providing insights into the pathogenesis of various human diseases.

Results

Clinical Samples and Pathology-Optimized Expansion Microscopy

We first devised a series of steps so that clinical samples could be converted to a state optimized for ExM processing (Fig. 1A and Supplementary Fig. 1). We considered three starting states: FFPE, H&E stained, and fresh frozen tissues, assuming the tissue to be thin-sliced and on a glass slide. We first investigated FFPE samples since we hypothesized that the steps required for the other categories would be subsets or permutations of the steps required for FFPE tissue processing. We evaluated whether xylene treatment to remove paraffin, followed by rehydration and a fairly standard antigen retrieval step (placing samples in 20 mM sodium citrate at pH 8 and 100°C, then immediately transferring the samples into a 60°C incubator for 30 mins; Supplementary Fig. 1), could sufficiently prepare FFPE samples for the proExM protocol[9]. In proExM, the succinimidyl ester of 6-((Acryloyl)amino)hexanoic acid (Acryloyl-X, SE; here abbreviated AcX) is used to chemically modify amines on biomolecules with an acrylamide functional group, which enables proteins to be linked to the polymer network; then, polymerization followed by proteinase K digestion (to an extent that spares the proteins of interest, e.g. applied antibodies) and addition of water enables expansion.

We found that heavily formalin-fixed human tissues (e.g., lymph nodes, skin, liver) did not expand evenly under the proExM protocol, even after paraffin removal, but if digestion was performed with 25 mM ethylenediaminetetraacetic acid (EDTA), vs. 1 mM as used in the original proExM protocol, we obtained excellent isotropic expansion with low autofluorescence (Supplementary Note, Supplementary Tables 1–2, and Supplementary Fig. 2A–2J). We validated the low distortion of this protocol on cultured cells using structured illumination super-resolution (SR-SIM) microscopy pre-expansion and confocal microscopy post-expansion (Supplementary Fig. 3). We next validated that this FFPE pipeline, with xylene treatment and increased EDTA, could prepare samples for proExM, by assessing the entire pipeline on normal human breast tissues prepared with FFPE preservation. We found that pre-expansion imaging with either a widefield (Fig. 1B) or SR-SIM (Fig. 1F) microscope, followed by post-expansion imaging on widefield (Fig. 1C) or confocal (Fig. 1G) microscopes respectively, yielded low distortion levels of a few percent (Fig. 1D, 1E, 1H, and 1I), similar to earlier ExM protocols[8,9]. Thus, this expansion pathology (ExPath) protocol was able to expand paraffin embedded, highly aldehyde-fixed samples.

We next sought to enable H&E-stained samples to be prepared for our enhanced proExM protocol. For mounted samples, we had to remove the cover slip and mounting medium; since we had established that xylene treatment was acceptable as a pre-treatment for ExM, we used xylene to remove the coverslip and dissolve away the mounting medium

(Supplementary Fig. 1). H&E stained tissues exhibited high background fluorescence (Supplementary Fig. 4), suggesting that removal of eosin and hematoxylin would be important for fluorescent antibody staining. We found that eosin and hematoxylin staining were both removed by ExPath processing (Supplementary Fig. 1 and 4). We visualized nuclear DNA in post-expansion H&E stained samples by DAPI staining (Fig. 1J, 1K), and applied antibody stains against the mitochondrial protein Hsp60 and stromal marker vimentin, using an H&E slide of human breast tissue with atypical ductal hyperplasia (ADH). Finally, we evaluated fresh frozen sections preserved with acetone fixation; we found that lowering the concentration of AcX from 0.1 mg/mL to 0.03 mg/mL enabled better processing (Supplementary Fig. 2K, 2L), perhaps because of the greater number of free amines in tissues not processed with aldehyde.

DNA fluorescent *in situ* hybridization (FISH) is commonly used to assess *ERBB2/HER2* gene amplification in breast cancer. We recently developed a method for expanding RNAs away from each other in biological samples and then accurately imaging their identity and location with RNA FISH[12]; here we examined whether post-expansion DNA FISH was possible. The large size of traditional bacterial artificial chromosome (BAC)-based FISH probes (e.g., the length of BAC-based FISH probes targeting *HER2* is approximately 220 kb) precludes efficient delivery to expanded samples, so we used commercially available SureFISH probes, which are libraries of single-stranded oligonucleotides with an average size of ~150 bases[13], targeting *HER2* and (as a control) the centrosome of chromosome 17. We observed that SureFISH probes diffused into breast ExPath samples and hybridized with chromosomal DNA, for specimens of breast cancers with no amplification of *HER2* (Fig. 1L) and for cancer with *HER2* amplification (Fig. 1M), with more DNA hybridization apparent in the *HER2*-amplified case. As DNA FISH is performed in the final step of the process, it does not interfere with immunostaining earlier in the protocol. We co-stained the breast samples with an antibody against HER2 protein, and confirmed the correlation of HER2 protein expression with *HER2* gene amplification (Fig. 1L, 1M).

ExPath, because it spaces apart molecules and also results in elimination of unanchored or digested molecules (such as non-antibody proteins that are digested by proteinase K treatment), has several advantages over conventional immunostaining. For example, tissue autofluorescence remains challenging for clinical applications of immunofluorescence and FISH in pathology analysis, despite existing autofluorescence reduction methods[14–16]. Specimens processed with ExPath are >99% water, and thus transparent and refractive index-matched to water. We observed substantially reduced autofluorescence from lung (Fig. 2A–J, wide-field fluorescent images) and breast (Fig. 2K–P, confocal fluorescent images) ExPath-processed specimens, when we compared signal to background (from regions selected by a pathologist's visual inspection), in spectral channels ranging from UV to red (Fig. 2Q, n=3 normal breast samples from different patients). Thus, the molecular clearing of ExPath, which eliminates unanchored biomolecules (including potentially both proteins as well as small molecules) that contribute to autofluorescence, can reduce autofluorescence by an order of magnitude in some spectral channels.

We applied ExPath to tissue microarrays containing specimens from various organs, including normal and cancer-containing tissues from breast, prostate, lung, colon, pancreas,

kidney, liver and ovary (Fig. 3), in all cases obtaining expansions of ~4–5x, with average expansion factor 4.7 (standard deviation (SD) 0.2; Supplementary Table 3). The expansion variation is smaller than 10%, indicating consistent performance of expansion across different types of human tissue. ExPath revealed sub-diffraction limit sized features of the intermediate filaments keratin and vimentin, critical in the epithelial-mesenchymal transition[17], cancer progression, and initiation of metastasis[18] (Fig. 3). An interesting future direction will be the examination of the nanoscale architecture of these and other proteins in the cellular and tissue context of cancer. We anticipate that ExPath will provide a simple and convenient way to observe nanoscale morphology of not only nucleic acids, but also protein biomarkers, in clinical biopsy samples from a wide range of human organs.

ExPath enables visualization of human podocyte tertiary foot processes

Many potential uses of ExPath are likely to be discovered by future exploration of normal vs. abnormal samples, followed by traditional or automated inspection of key features, both for pinpointing novel pathological mechanisms, as well as for disease classification and refined diagnosis. However, there are some scenarios where nanoscopic resolution is already necessary. For example, nephrotic kidney diseases such as minimal change disease (MCD) and focal segmental glomerulosclerosis (FSGS) are typically diagnosed or confirmed via EM[19,20]. In MCD, kidney tertiary podocyte foot processes, which normally cover the surface of glomerular capillary loops like interdigitating fingers, lose their characteristic morphology and appear continuous under EM – a phenomenon called foot process effacement[10]. The width of individual foot processes is around 200 nm, beyond the resolution of conventional optical microscopy[21].

Here, we explored whether ExPath could enable imaging of podocyte foot processes. We identified an anti-actinin-4[22] and an anti-synaptopodin[23] antibody that each could specifically label tertiary podocyte foot processes in acetone-fixed frozen kidney samples that were heat-treated prior to immunostaining (Supplementary Figs. 5 and 6). The quality of immunostaining of anti-actinin-4 slightly decreased for kidney samples that were FFPE-preserved (Supplementary Fig. 7), compared to that of acetone-fixed frozen kidney samples, presumably due to degraded antigenicity caused by formalin. We stained human kidney samples with anti-actinin-4, as well as antibodies against vimentin (a glomerular marker), and collagen IV (a capillary basement membrane marker), and successfully observed the microanatomy of glomeruli (Fig. 4A vs. B) post-expansion, revealing ultrafine structures of tertiary podocyte foot processes (Figs. 4B, 4C) not visible in confocal imaging (Fig. 4A), in normal human kidney samples. We acquired ExPath images of fresh-frozen kidney sections from individuals with normal kidneys, as well as from patients with MCD and FSGS. We observed the ultrafine structure of tertiary foot processes in kidneys from normal cases (Fig. 4E), as well as foot process effacement in MCD cases (Fig. 4G), consistent with the morphologies seen in EM images from the same samples (Fig. 4D and 4F). Thus, nanoscale differences between clinical samples of nephrotic diseases could be visualized with diffraction-limited optical microscopes with ExPath.

To examine in a blinded study whether ExPath could enable accurate identification of foot process effacement in MCD and FSGS cases, seven observers, including four pathologists

and three non-pathologists, first studied a training set of immunofluorescent images of kidney glomeruli in both pre-expansion and post-expansion states (see full image set in Supplementary Fig. 8), then examined 10 pre-expansion and 10 post-expansion immunofluorescence images of kidney glomeruli from 3 specimens from normal subjects, 2 specimens from MCD patients and 1 specimen from an FSGS patient (Supplementary Fig. 8 and Supplementary Table 4). For unexpanded samples, classification accuracy was only 65.7% (standard deviation (SD) 17%), but increased significantly to 90% (SD 8%) when ExPath samples were used (p=0.0088, two tailed t-test; raw data in Supplementary Table 5). To assess inter-observer agreement, we calculated Fleiss's kappa values for observers' categorical ratings on pre- vs. post-expansion images. Observers' ratings of post-expansion data were consistent, with kappa value 0.68±0.14 at the 95% confidence level, whereas inter-observer agreement was poor on pre-expansion data (0.35±0.13, 95% confidence level; this value was borderline, given the clinically acceptable threshold of 0.40)[24]. ExPath enabled accurate and consistent evaluation among observers on whether the image was from a sample in a normal or abnormal state, from a single post-expansion image (in clinical practice, kidney pathologists normally examine multiple EM images for diagnosis). Our results suggest that large-scale blinded studies using ExPath, although beyond the scope of the current technology-oriented paper, may be relevant for streamlining the diagnosis or confirmation of nephrotic kidney disease, and potentially other diseases that involve known nanoscale pathology, as well as helping detect diseases earlier when the changes are too small to be resolved with ordinary microscopes.

ExPath improves computational diagnosis in early breast lesions

To further explore the utility of ExPath, we examined the pathological classification of early breast lesions, which represents one of the most challenging problem areas in breast pathology[11]. For example, one study has shown that there is only ~50% agreement for nuclear atypia diagnosis in early breast lesions[11]. The classification of these lesions provides critical diagnostic information to prevent over- and under-treatment, and to guide clinical management[25,26].

We hypothesized that the problems with the current classification schemes are due to two issues: first, the diagnostic criteria are largely qualitative and subjective; second, the information contained in the images is limited by the optical diffraction limit of conventional optical microscopes. To start addressing the first issue, we previously developed computational pathology models that can discriminate benign from malignant intraductal proliferative breast lesions[27]. However, the efficacy of these models is limited by the information extractable from diffraction-limited images. Because ExPath substantially increases image resolution, we anticipated that the extra information enabled by ExPath could lead to a higher quality of extracted features, and thus improve the classification of pre-invasive breast lesions.

We applied our previously developed image classification framework[27] on ordinary H&E-stained samples, as well as an image classification framework updated with nucleus detection and segmentation algorithms optimized for post-expansion DAPI-stained images (Fig. 5A). Our image classification framework for post-expansion DAPI-stained images

includes foreground detection, nucleus seed detection, and nuclear segmentation (Fig. 5A). Following application of this framework, we extract three kinds of features from each segmented nucleus from both the pre-expanded and post-expanded images: nuclear morphology features, nuclear intensity features, and nuclear texture features.

Each of the two datasets (pre- and post-expansion) consists of 105 images: 36 normal breast tissue images, 31 proliferative lesion (benign) images (15 usual ductal hyperplasia (UDH), 16 atypical ductal hyperplasia (ADH)) and 38 ductal carcinoma in situ (DCIS). The average expansion factor was 4.8 (SD: 0.3). We first assessed the impact of ExPath on nuclear detection and segmentation, for a subset of 31 images (6 normal, 9 UDH, 9 ADH and 7 DCIS; Fig. 5B). Computational detection of nuclei was significantly more accurate in expanded samples (Fig. 5B), with an 11% increase in true positive rate, 22% increase in positive predictive value, and 16% increase in f-score, over non-expanded samples (Supplementary Tables 6 and 7; Supplementary Fig. 9), and segmentation was significantly improved as well, with a 14% increase in f-score, 77% increase in Cohen's kappa and 66% decrease in global consistency error (GCE) (Supplementary Table 8). This improved accuracy of nuclear detection and segmentation could in principle support improved computational pathology analyses. To this end, we found that expansion substantially improved the performance of diagnosis classification models over pre-expansion data (Fig. 5C; Supplementary Table 9). When we examined the area under the receiver operator curve (AUC) of true positives vs. false positives - a perfect classifier should achieve an AUC of 1, and a random classifier would achieve an AUC of 0.5- our pipeline was able to discriminate lesions such as UDH from atypical lesions such as ADH with an AUC of 0.93 on expanded samples, compared with only 0.71 on pre-expanded samples. The most significant features selected by these classification models are shown in Supplementary Tables 10 and 11. Features extracted from individual post-expansion images were normalized by their expansion factors, before running our digital pathology pipeline; however, such normalization did not affect the results greatly (Supplementary Table 12). These findings suggest that the improved nuclear segmentation achieved on post-expansion images results in more informative features and in turn higher-performing classification models.

Discussion

We herein describe ExPath, a simple and versatile method for optical interrogation of clinical biopsy samples with nanoscale precision and molecular information. ExPath is an extension of our proExM protocol[9] that is optimized for clinical samples -FFPE, H&E stained, and fresh frozen tissues. ExPath thus enables nanoscale imaging on common imaging hardware. We found that ExPath functions well on a wide diversity of tissue types, and that it has immediate clinical application in the diagnosis of diseases known to exhibit nanoscale pathology (e.g., kidney MCD). Although EM has far superior resolution compared to ExPath, the processing time for ExPath is significantly shorter than that for EM, and the requirement for skills and equipment to perform ExPath is much less demanding vs. those required for EM (Supplementary Table 13). Moreover, ExPath enables multiplexed localization and identification of biomolecules *in situ*, which is challenging with EM. Of course, without larger-scale studies it is unclear whether ExM would eliminate the need for EM in diagnostic renal pathology of podocytopathies. We highlight the potential of

ExPath to improve diagnostics by providing greater information content to inform sample classification. We found that ExPath enhances the ability to detect and segment nuclei, and the increased information content of expanded breast tissue samples improves the performance of computational pathology classifiers for the analysis of proliferative breast lesions.

ExM protocols are robust: in parallel to our development of proExM, two other groups developed similar protocols[28,29], highlighting the ability of multiple groups to implement such technologies. Another key advantage of ExPath is its versatility: we demonstrate here that we can not only address a wide variety of samples, but adopt ExPath to multimodal investigation of clinical samples, e.g. incorporating DNA FISH into the pipeline easily, using only commercially available probes. In the future, it will be of interest to combine ExPath with ongoing developments in multiplexed imaging of RNA[30–32] and protein[33]. Although embedding biological specimens in hydrogels such as polyacrylamide to support imaging goes back decades[34], the use of polyelectrolyte hydrogels to move biomolecules and labels apart evenly may help support chemical analysis of biomolecules in situ, since expansion microscopy separates biomolecules and surrounds them by pure environments of our choosing.

ExPath, in the current iteration, enables ~4.5x physical magnification in each dimension. Although it expands the volume to be imaged, and thus requires more voxels to be imaged, the ability to use fast diffraction limited optics enables the voxel sizes of a super-resolution imaging modality to be acquired at the voxel acquisition rates of fast diffraction limited optics. ExPath is compatible with a wide variety of stains and antibodies used throughout biology and pathology. Similar to ExM and proExM, ExPath samples are transparent with a refractive index matched to water, and thus can support fast volumetric imaging on lightsheet microscopes (as has been previously shown for expanded samples[35]). In the current implementation of ExPath, most proteins are digested away to enable even expansion, preventing post-expansion interrogation. In the future, protein retention forms of ExM that enable most proteins to be retained[9,34] may support more information-preserving forms of ExPath. To date, these “full protein retention” forms of ExM have not been fully validated by direct comparison to a classical super-resolution modality. Another property of ExPath is that the expansion process dilutes the concentration of fluorophores. For low abundance targets, it may be desirable to implement signal amplification prior to imaging. Since proteins are lost after proteinase K treatment,non-protein-reliant amplification methods, such as hybridization chain reaction amplification of gel-anchored labels, may be helpful, as has been demonstrated for single-molecule RNA imaging in expanded specimens[35].

Standardization and automation of ExPath are important future steps toward clinical adoption. Comparing pre- and post-expansion images taken at low magnifications enables simple calculation of the expansion factor, so that the physical size of the post-expansion image can be mapped onto biologically relevant units, and nulling out the small (<10%) sample-to-sample variation of expansion factor.

ExPath is particularly poised to enhance the computational analysis of pathological specimens. Here, we analyzed nuclear morphology and explored the classification of early breast lesions. We found that nuclear segmentation algorithms, which historically have shown only moderate performance on standard histopathological images[36], show excellent performance on ExPath images. We also find that diagnosis classification models that focus on nuclear morphologic phenotypes perform better on ExPath images than on pre-expansion images. The accurate classification of pre-invasive breast diseases represents a difficult area in diagnostic pathology with significant discordance observed between individual pathologists[11]. Accurate classification is importantbecause it determines clinical treatment which can range from observation (for a benign non-atypical lesion) to surgery (for a diagnosis of atypia or malignancy). Further validation of our findings on larger sets of samples will be critical towards understanding the potential of this technology in the clinic. We envision that it will be possible to integrate ExPath with computational pathology for computer assisted interpretation of biopsies. In general, as cancer screening procedures for common malignancies continue to improve (e.g. skin, lung, prostate, esophagus, colon), a larger proportion of pathology specimens will contain small, non-invasive lesions, and accurate pathological classification of these specimens will play an important role in clinical management.

METHODS

Methods and any associated references are available in the online version of the paper.

ONLINE METHODS

Human samples

The breast pathological specimens used in Figure 1J and K and 9 cases from the study on ExPath-based analysis of early breast lesions (Fig. 5) were from the pathology archives of the Beth Israel Deaconess Medical Center, obtained under BIDMC IRB protocol #2013p000410 to A.H.B (In addition, we used 11 cases from US Biomax and 21 cases from Abcam.). The frozen kidney pathological samples used in Figure 4D–G and Supplementary Figure 8 were provided by the Brigham and Women's Hospital archives under the BWH IRB protocol #2011P002692 to A.W. The rest of the breast and kidney samples used in this study were bought from either US Biomax or Abcam (Supplementary Table 14). Other human tissue samples and tissue microarrays were purchased from commercial sources (see Supplementary Table 14). The use of unused, unidentified archival specimens does not require informed consent from the subjects.

Tissue section recovery

For formalin-fixed paraffin-embedded (FFPE) clinical samples, samples were placed in a series of solutions sequentially, 3 mins for each step: 2× xylene, 2× 100% ethanol, 95% ethanol, 70% ethanol, 50% ethanol, and finally doubly deionized water. All the steps were performed at room temperature (RT), 3 mins each.

For stained and mounted permanent slides, samples were briefly placed in xylene at RT. Then coverslips were carefully removed with appropriate tools, such as a razor blade. If the

coverslip was difficult to remove, the slides were further incubated in xylene at RT until the coverslip was loosened. Slides were then treated as FFPE samples.

Unfixed frozen tissue slides in optimum cutting temperature (OCT) solution (Tissue-Tek) were initially fixed for 10 min in acetone at −20°C before three PBS washes for 10 min each at RT. For already-fixed frozen clinical tissue sections, the slides were left at RT for 2 min to let the OCT melt, and washed 3x with PBS solution at RT for 5 min each.

Sample heat treatment

All human tissue samples used in this study were heat treated prior to immunostaining. Briefly, tissue slides were placed in 20 mM sodium citrate solution (pH 8 at ~100°C, in a heat-resistant container, and then the container was immediately transferred to a 60°C incubator for 30 min.

Immunostaining

Samples were first blocked with MAXblock™ Blocking Medium (Active Motif) for 1 hour at 37 °C, followed by incubation with primary antibodies in MAXbind™ Staining Medium (Active Motif) at a concentration of 10 μg/mL for at least 3 h at RT or 37 °C (in our hands, it did not matter which), and then washed 3 times with MAXwash™ Washing Medium (Active Motif) for 10 minutes each at RT. Samples were incubated with appropriate secondary antibodies at a concentration of approximately 10 μg/mL together with 300 nM DAPI (if DAPI was used; DAPI was from Thermo Fisher Scientific) in MAXbind™ Staining Medium for at least 1 h at 37 °C, for 5 μm thick tissue (further optimization of incubation duration or temperature may be needed for thicker tissues), then washed in MAXwash™ Washing Medium 3 times for 10 min each at RT. All the primary antibodies used in this work are listed in Supplementary Table 15. Secondary antibodies used were: goat anti-chicken Alexa 488 (Life Technologies), goat anti-rabbit Alexa 546 (Life Technologies) and goat anti-mouse CF633 (Biotium), except that goat anti-guinea pig Alexa 488 (Life Technologies) was used in Supplementary Figure 6, goat anti-mouse Atto 647N (Life Technologies) was used in Figure 3, and goat anti-chicken Alexa 546 (Life Technologies) and goat anti-rabbit Alexa 488 (Life Technologies) were used in Figure 4.

Chemical treatment for protein preservation

The expansion microscopy method used is a variation of our previously reported proExM protocol[9]. Acryloyl-X, SE (6-((acryloyl)amino)hexanoic acid, succinimidyl ester, here abbreviated AcX, fromThermo Fisher Scientific) was dissolved in anhydrous DMSO at a concentration of 10 mg/mL, then aliquotted and stored frozen in a desiccated environment at −20 °C. Tissue slides were incubated with 0.03–0.1 mg/ml AcX (0.03 mg/ml for samples fixed with non-aldehyde fixatives, 0.1 mg/ml for samples fixed with aldehyde fixatives), diluted in PBS buffer, for at least 3 hours at RT. Note that thicker samples require longer incubation times.

In situ polymer synthesis

The method for *in situ* polymer synthesis in ExPath is slightly modified from our original proExM protocol[8]. Briefly, a monomer solution made of 1x PBS, 2 M NaCl, 8.625% (w/w)

sodium acrylate, 2.5% (w/w) acrylamide, 0.10% (w/w) N,N′-methylenebisacrylamide (or BIS for short) (all from Sigma Aldrich), was prepared and aliquotted and stored at −20 °C prior to *in situ* polymer synthesis. The slightly lower BIS concentration caused slightly more expansion than previous protocols, at the expense of slightly lower gel sturdiness. The chemicals 4-hydroxy-2,2,6,6-tetramethylpiperidin-1-oxyl (4HT, Sigma Aldrich) as an inhibitor, tetramethylethylenediamine (TEMED, Sigma Aldrich) as an accelerator and ammonium persulfate (APS, Sigma Aldrich) as an initiator, were added sequentially to the monomer solution each to prepare the gelling solution (final concentration: 0.01% (w/w) for 4HT and 0.2% (w/w) for both APS and TEMED). Tissue slides were incubated with the monomer solution for 30 mins at 4°C to allow diffusion of monomer solution into the tissues, while preventing premature gelation. Then, a gel chamber was constructed by putting a coverslip on top of the tissue, with spacers on either side of the tissue section to prevent compression of tissue. The gel chamber was filled with the fresh gelling solution. Finally, slice samples were incubated for 1.5–2 hours at 37 °C in a humidified atmosphere, to complete gelation.

Sample digestion and expansion

After gelation, samples were incubated in 8 U/ml proteinase K (New England Biolabs) in a digestion buffer (modified from the original proExM recipe) consisting of 50 mM Tris (pH 8), 25 mM EDTA, 0.5% Triton X-100, 0.8 M NaCl, and the tissues were incubated for 3 hours at 60°C or until the completion of digestion (i.e., the gelled tissue is detached from the glass slide and becomes transparent, and the gelled tissue remains flat without bending or twisting in the solution). Digested samples were washed once with 1x PBS buffer for 10 min at RT and stained with 300 nM DAPI in PBS buffer for 20 mins at RT, then washed once with 1x PBS for 10 min at RT. Finally, gels were placed in doubly deionized water at RT for 10 min to expand. This step was repeated 3–5 times in fresh water until the size of the expanded sample stabilized. To prevent bacterial growth, we sometimes added sodium azide (final concentration 0.002% – 0.01%) to the water used for expansion. Note that additional of sodium azide may reduce the expansion factor, however, by around 10%.

Structured illumination microscopy pre-expansion imaging

For Supplementary Fig. 3, HeLa cells (ATCC CCL2) were fixed with 4% paraformaldehyde for 10 min, washed 3 times for 5 minutes each with PBS, and permeabilized with 0.1% Triton X-100 for 15 min. Microtubules in fixed HeLa cells were stained with primary antibodies (rabbit anti-α-tubulin, Abcam) in MAXbind™ Staining Medium (Active Motif) at a concentration of 10 μg/mL for 1–4 hours at 37 °C and then washed in MAXwash™ Washing Medium (Active Motif) three times for 5 min each. Specimens were then incubated with secondary antibodies and 300 nM DAPI in MAXbind™ Staining Medium for 1–4 hours at 37°C and then washed in PBS 3 times for 5 min each These cells were used as a technology testbed, not to make scientific conclusions, so no detailed scientific justification for the choice of cell line is needed. Cells were authenticated and tested for mycoplasma contamination via standard procedures of the ATCC. Unless specifically stated, all the steps were performed at RT.

For Figure 1F, a customized 5 μm thickness breast TMA was prepared and stained with primary (rabbit anti-KRT19, chicken anti-vimentin) as well as secondary antibodies and DAPI as described in the “Immunostaining” section. Super-resolution structured illumination microscopy imaging was performed on a Deltavision OMX Blaze (GE Healthcare) SIM microscope with a 100x 1.40 NA (Olympus) oil objective. Stained samples were imaged with SlowFade Gold (Invitrogen) antifade reagent for suppression of photobleaching and refractive index matching for pre-expansion imaging.

Fluorescent microscopy after expansion

Low-magnification images of specimens (Fig. 1B, 1C, “Core” images of Fig. 3, Supplementary Figs. 2E–H, 4, and 5) were imaged on a Nikon Ti-E epifluorescence microscope with a SPECTRA X light engine (Lumencor) and a 5.5 Zyla sCMOS camera (Andor), controlled by NIS-Elements AR software, with a 4× 0.13 NA air objective or 10× 0.2 NA air objective (Nikon). For Figures 1K–M, Figure 2A–J, Figure 5, Supplementary Figures 2Aii, Aiii, Av, Avi, Bii, Biii, Bv, Bvi, 2I–J, 6 and 8, the images were acquired on the same microscope with a 40× 1.15 NA water immersion objective (Nikon). The following filter cubes (Semrock, Rochester, NY) were used: DAPI, DAPI-11LP-A-000; Alexa Fluor 488, GFP-1828A-NTE-ZERO; Alexa Fluor 546, FITC/TXRED-2X-B-NTE; Atto 647N or CF 633, Cy5-4040C-000.

All other fluorescent images were taken on an Andor spinning disk (CSU-X1 Yokogawa) confocal system on a Nikon TI-E microscope body, with a 40× 1.15 NA water immersion objective. DAPI was excited with a 405 nm laser, and imaged with a 450/50 emission filter. Alexa Fluor 488 was excited with a 488 nm laser, and imaged with a 525/40 emission filter. Alexa Fluor 546 was excited with a 561 nm laser and imaged with a 607/36 emission filter. Atto 647N and CF633 were excited with a 640 nm laser and imaged with a 685/40 emission filter.

To prevent the gels from drifting during imaging following expansion, they were placed in glass bottom 6-well plates with all excess liquid removed. If immobilization was needed, liquid low melt agarose (2% w/w) was pipetted around the gel and allowed to solidify, to encase the gels before imaging.

Figure 1G, Figure 2, Figure 3 (except core images), Figure 4, Supplementary Figure 7 and Supplementary Figure 9 are maximum intensity projections (MIPs) of 0.25 μm thickness (in pre-ExM distance units). Figure 1K–M, Figure 5 and Supplementary Figure 8 are MIPs of 2 μm thickness.

Brightfield microscopy

Low magnification images (Supplementary Fig. 4) were acquired on a Nikon Ti-E microscope with a DS-Ri2 sCMOS 16mp Color Camera (Nikon) and white LED illuminator, with a 4× 0.13 NA air objective or 10× 0.2 NA air objective. High magnification images of H&E slides (Fig. 1J, Fig. 5, and Supplementary Fig. 9) were acquired on the Panoramic Scan II (3DHistech), with a 40× 0.95 NA air objective (Zeiss).

Autofluorescence analysis

Background was removed from images by subtraction of mean pixel values from blank regions, prior to analysis. For each fluorescent channel, 10 regions of interest containing the brightest fluorescent signals and one area containing only autofluorescence signal, as judged by a pathologist's visual inspection, were selected, and used to calculate signal-to-background ratios.

Measurement of the expansion factor and normalization

We suggest, as we did here, that users acquire low magnification images of the sample pre- and post-expansion, and then take the ratio of these sizes to calculate the expansion factor, which can be used to normalize the physical size of the post-expansion image to that of the pre-expansion state, and thus enable "biological" length units to be utilized. This normalization process also nulls out the small (<10%) natural sample-to-sample variability of the expansion process.

Measurement error quantification

This section is based on our previously described method[8] for distortion vector field calculation and root-mean-square (RMS) error calculation, with minor modifications. We semi-automated the distortion vector field and RMS error calculation with improved code, eliminating the need for manual selection of control points for the non-linear registration that leads to the distortion vector field[8]. Given the challenge of finding matching z planes in pre- vs. post-expansion states, the same fields of view in multiple z planes were first imaged pre- and post-expansion. To match z planes pre- and post-expansion, scale-invariant feature transform (SIFT) keypoints[37] were generated for all the possible combination of pairs of pre-expansion z planes and post-expansion z projections (note that since the sample expands along the z axis, 1 pre-expansion z plane should correspond to 1 post-expansion z projection from 4–5 z planes). SIFT keypoints were generated using the VLFeat open source library[38] and filtered by random sample consensus (RANSAC) with a geometric model that only permits rotation, translation, and uniform scaling. The pair of pre- and post-expansion images with the most SIFT keypoints was used for image registration by rotation, translation and uniform scaling, as well as calculation of expansion factors and distortion vector fields. By subtracting the resulting vectors at any two points, distance measurement errors could easily be sampled, and the RMS error for such measurements was plotted as a function of measurement length from at least 3 patients.

Expansion immunoFISH

For ExPath samples being processed for immunohistochemistry plus DNA FISH probing, digested gel samples were placed in hybridization buffer made of 1× PBS, 15% ethylene carbonate, 20% dextran sulfate, 600 mM NaCl and 0.2 mg/ml single stranded salmon sperm DNA at 85°C for 30 mins, then mixed with 30 μL of hybridization buffer containing SureFISH probes 17q12 HER2 and Chr17 CEP (Agilent/Dako) which was pre-heated at 85 °C for 10 mins. The mixtures were then incubated at 45°C overnight. The next day, samples were washed with stringency wash buffer made of 1×SSC (150 mM NaCl, 15 mM sodium citrate, pH 7.0) and 20% ethylene carbonate at 45°C for 15 min, followed by washes

with 2× SSC at 45 °C, 3 times for 10 mins each. Finally, the gel samples were washed with 0.02× SSC multiple times at RT (5 min each) until the expansion was completed.

Computational nuclear atypia analysis

For the task of evaluating Nucleus Detection and Nucleus Segmentation, the analyses leading to the tables and figures listed below used 31 cases out of the total of 105 cases: Supplementary Table 6; Supplementary Table 7; Supplementary Table 8; Supplementary Fig. 9. For the task of Image Classification (see corresponding section below), the tables and figures below used all 105 cases: Supplementary Table 9; Supplementary Table 10; Supplementary Table 11; Supplementary Table 12; Figure 5C. We proposed a framework for classification of expanded tissue images into different categories: normal breast, benign breast lesions (UDH and ADH), and non-invasive breast cancer (DCIS). This image classification framework consisted of four components: image preprocessing, nuclei segmentation, feature extraction and image classification. The image pre-processing and nuclei segmentation pipelines are shown in Figure 5A.

Image pre-processing

Due to confocal acquisition (see above) of multiple non-overlapping image tiles which required stitching to produce a single image, these tiles exhibited background fluorescent signals. During image pre-processing, a rolling-ball algorithm[39] with ball size set to the average nuclei size was applied to remove background noise. After background noise removal, nucleus-to-background contrast was enhanced by adaptive histogram equalization[40]. These enhanced images were then smoothed by a median filter with radius 10.

Nuclei Segmentation

The nuclei segmentation procedure consisted of three steps. First, nuclei were segmented using a Poisson distribution based minimum error thresholding method[41]. Standard and global thresholding methods are not efficient as a minimum error threshold method, because of the high variability within the nuclei regions and background regions. In order to address this issue, our locally adaptive thresholding algorithm selected the threshold by modelling the image histogram as a mixture of two Poisson models. The threshold value was computed by minimizing the relative entropy between the image histogram and the Poisson mixture model. The initial segmentation of nuclei was then improved by a set of morphological operations that include hole-filing and morphological closing to fill holes and to combine small fragments of nuclei into single nuclei, and morphological opening to remove small non-nucleus regions (e.g. blood vessels, parts of fragmented nuclei, and artifacts). This segmentation method may under-segment clusters of nuclei that touch each other. Second, to separate the touching and overlapping nuclei, we used a scale-adaptive multi-scale Laplacian of Gaussian (MSLoG) filter[42] to produce local maxima and select seed points for nuclei. For selecting local maxima, constant scale produces imprecise nuclear seed points, since nuclear size varies considerably in early breast neoplasia lesions. In order to address this problem, a scale-adaptive MSLoG filter was applied on a given number of scales, and then local maximum points in the scale-space response were selected as seed points. Last, these seed

points were used as markers for the marker-controlled watershed algorithm to separate touching and overlapping nuclei.

Feature extraction

After nuclei segmentation, we extracted morphological, first-order statistical and second-order statistical features for each nucleus. The morphological features included shape and geometrical features which reflect nuclear phenotypic information. The computed morphological features were: area, convex area, perimeter, equivalent perimeter, eccentricity, orientation, solidity, extent, compactness, major axis length, minor axis length, elliptical minor, and major radius. The first-order statistical features corresponded to the distribution of gray-level values within nuclei. The computed first-order statistical features were: mean, median, mean absolute deviation, standard deviation, interquartile range, skewness, and kurtosis. The second-order statistical features corresponded to the textural variation inside nuclei.

We computed two types of second order statistical features using grey level Haralick co-occurrence[43] and run-length[44] matrices. The co-occurrence matrix GLCM ($i,j; d,\theta$) is square with dimension Ng where Ng is the total number of grey levels in the image. The value at the ith column and jth row in the matrix was produced by counting the total number of occasions where a pixel with value i is adjacent to a pixel with value j at a distance d and angle θ. Then the whole matrix was divided by the total number of such comparisons that were made. Alternatively, we can say that each element of the GLCM matrix is considered as the probability that a pixel with grey level i is to be found with a pixel with grey level j at a distance d and angle θ. We defined adjacency in four directions (vertical, horizontal, left and right diagonals) with one displacement vector, which produced four GLCM matrices. In our case, texture information was rotationally invariant. So, we took the average in all four directions and produced one GLCM matrix. Later, we computed 14 features proposed by Haralick from the GLCM in order to identify texture more compactly. These 14 features were: Autocorrelation, Correlation, Contrast, Cluster Shade, Cluster Prominence, Energy, Entropy, Homogeneity, Inverse Difference Normalized, Inverse Difference Moment Normalized, Dissimilarity, Maximum Probability, Information Measure Correlation 1 and Information Measure Correlation 2.

The set of consecutive pixels, with the same grey level, collinear in a given direction, constitutes a grey level run length matrix GLRLM ($i,j; \theta$). The dimension of the GLRLM is $Ng \times R$, where Ng is the number of grey levels and R is the maximum run length. Similar to the GLCM, we computed GLRLMs for four directions and averaged them. The 11 run-length features, derived from the GLRLM, are: short run emphasis (SRE), long run emphasis (LRE), grey-level non-uniformity (GLN), run length non-uniformity (RLN), ratio-percentage (RP), low grey level runs emphasis (LGLRE), high grey level runs emphasis (HGLRE), short run low grey level emphasis (SRLGLE), short run high grey level emphasis (SRHGLE), long run low grey level emphasis (LRLGLE) and long run high grey level emphasis (LRHGLE). In total, we computed 45 features for each nucleus. Last, these features were summarized at the image level by computing the first-order statistics including

mean, median, mean absolute deviation, standard deviation, interquartile range, skewness and kurtosis of each feature per image, producing 315 summary features per image.

Image classification

In the last part of our framework, we performed logistic regression with Lasso regularization to build multivariate image feature-based models to classify normal, benign and pre-invasive malignant tissue images. The analyses were implemented in R (http://www.r-project.org/), using the glmnet package[45]. Lasso regularization[46] was used to create simpler models, less prone to overfitting than those that would be obtained from standard logistic regression. The Lasso procedure consists of performing logistic regression with an L1 regularization penalty, which has the effect of shrinking the regression weights of the least predictive features to 0. The amount of the penalty (and the number of non-zero features in the model) is determined by the regularization parameter λ. This method has been shown to perform well in the setting of colinearity[47] and has been widely used to build predictive models from high-dimensional data in translational cancer research. Features were standardized separately in the training and validation data-sets prior to model construction, using the selected setting in glmnet. We evaluated model performance with 6-fold cross validation (6F-CV). For validation, we selected the value of λ that achieved the maximum area under curve (AUC) in cross-validation on the training data-set and applied this fixed model to the validation data-set. Model performance was assessed by computing the AUC of true positives vs. false positives, where a perfect classifier would achieve an AUC of 1, and a random classifier would achieve an AUC of 0.5.

We also evaluated our framework using two other machine learning classifiers, which are commonly used in biomedical research. A random forest classifier[48] fits a number of decision trees on various sub-samples of the dataset and uses averaging to improve the predictive accuracy and to control over-fitting. Number of trees (numTrees), maximum depth of the tree (maxDepth) and number of features (numFeatures) to be used in random selection are three parameters that affect the performance of the random forest classifer. In our experiments we used numTrees = 100, maxDepth=30 and numFeatures=20. The other classifier we explored was Naïve Bayes[49], which is a probabilistic classifier based on applying Bayes' theorem with strong independence assumptions between the features. As the predicted value is class label (e.g., we are pursuing a classification problem), the independence assumption is less restrictive for classification as compared to regression[51].

Image classification results

We applied our image classification framework on both pre-expanded and expanded images. Both data sets consisted of 105 images containing 36 normal breast tissue images, 31 non-invasive lesion breast tissue images (15 UDH and 16 ADH) and 38 pre-invasive breast tissue images (DCIS) from 41 cases (likely different patients, but since patients were identified only by sex and age in commercial samples, this is a lower bound). Thus, these 105 images belonged to 4 different classes (Normal, UDH, ADH and DCIS). The ground-true classification was performed and validated by 3 certified pathologists (E.Y.O., V.T., and S.J.S.) from more than 350 examined cases. The total number of images was 131; 105 images were analyzed and 26 were excluded because they were judged to be borderline

diagnostic cases. In order to discriminate normal breast tissue vs. non-invasive and pre-invasive breast tissues, we performed binary classification for all classes (Fig. 5C). When discriminating normal breast tissue vs. UDH, ADH and DCIS tissue, the GLMNET classifier reported AUC values of 0.95, 0.96 and 0.94 for expanded data as compared to AUC values of 0.86, 0.82 and 0.75 for pre-expanded data, respectively. For differentiating non-atypical breast tissue (UDH) from atypical breast tissues (ADH and DCIS), the GLMNET classifier reported AUC values of 0.93 and 0.89 for expanded data as compared to AUC values of 0.71 and 0.82 for pre-expanded data, respectively. For discriminating atypical benign breast tissue (ADH) vs. pre-invasive breast cancer tissue (DCIS), the GLMNET classifier reported a AUC value of 0.95 for expanded data as compared to a AUC value of 0.84 for pre-expanded data. A comparison of GLMNET classification results vs. two other machine learning classifiers (Naïve Bayes and Random Forest) is reported in Supplementary Table 9. Top performing features in expanded and pre-expanded data are reported in Supplementary Tables 10 and 11, respectively.

Statistical analysis

Statistical analyses were performed with R (version 3.2.5). Data are presented as mean ± standard deviation (SD) or standard error of the mean (SEM) with sample numbers n noted in the text, tables, and figure legends. Student's t-test was used to determine significant differences between means. A bootstrapped paired t-test was used to statistically compare receiver operator curves. In the box plot graphs, the ends of whiskers are defined by the SD, and the central rectangle spans from minimum to maximum; the segment in the rectangle indicates the median, and the square symbol indicates the mean.

Data availability

The Expansion Pathology protocol and the code used for the computational nuclear atypia analysis are posted at http://expansionmicroscopy.org. Data are available upon request to the corresponding authors of the paper.

Supplementary Material

Refer to Web version on PubMed Central for supplementary material.

Acknowledgments

For funding, E.S.B. acknowledges the MIT Media Lab, the Open Philanthropy project, the HHMI-Simons Faculty Scholars Program, U. S. Army Research Laboratory and the U. S. Army Research Office under contract/grant number W911NF1510548, the MIT Brain and Cognitive Sciences Department, the New York Stem Cell Foundation-Robertson Investigator Award, NIH Transformative Award 1R01GM104948, NIH Director's Pioneer Award 1DP1NS087724, NIH 1R01EY023173, NIH 1U01MH106011, NIH 1R01MH110932, and the MIT McGovern Institute MINT program. A.H.B. acknowledges the support from Harvard Catalyst, The Harvard Clinical and Translational Science Center (National Center for Research Resources and the National Center for Advancing Translational Sciences, National Institutes of Health Award UL1 TR001102) and financial contributions from Harvard University and its affiliated academic healthcare centers. A.H.B. and O.B. also acknowledge support from the Ludwig Center at Harvard, and the Ludwig's members Dr. Joanne Brugge and Dr. Jane Staunton. O.B. acknowledges the Lady Tata Memorial Trust, London, UK. F.C. acknowledges the NSF Fellowship and Poitras Fellowship.

References

1. Huang B, Bates M, Zhuang X. Super-resolution fluorescence microscopy. Annu Rev Biochem. 2009; 78:993–1016. [PubMed: 19489737]
2. Huang B, Babcock H, Zhuang X. Breaking the diffraction barrier: Super-resolution imaging of cells. Cell. 2010; 143:1047–1058. [PubMed: 21168201]
3. Hell SW. Far-field optical nanoscopy. 2010 23rd Annual Meeting of the IEEE Photonics Society, PHOTINICS 2010. 2010; :3–4. DOI: 10.1109/PHOTONICS.2010.5698725
4. Hell SW. Toward fluorescence nanoscopy. Nat Biotechnol. 2003; 21:1347–55. [PubMed: 14595362]
5. Phelps PE, Houser CR, Vaughn JE. Immunocytochemical localization of choline acetyltransferase within the rat neostriatum: a correlated light and electron microscopic study of cholinergic neurons and synapses. J Comp Neurol. 1985; 238:286–307. [PubMed: 4044917]
6. Nixon RA, et al. Extensive Involvement of Autophagy in Alzheimer Disease: An Immuno-Electron Microscopy Study. J Neuropathol Exp Neurol. 2005; 64:113–122. [PubMed: 15751225]
7. Gaietta G, et al. Multicolor and electron microscopic imaging of connexin trafficking. Science. 2002; 296:503–507. [PubMed: 11964472]
8. Chen F, Tillberg PW, Boyden ES. Expansion microscopy. Science. 2015; 347:543–548. [PubMed: 25592419]
9. Tillberg PW, et al. Protein-retention expansion microscopy of cells and tissues labeled using standard fluorescent proteins and antibodies. Nat Biotechnol. 2016; 34:987–992. [PubMed: 27376584]
10. Waldman M, et al. Adult Minimal-Change Disease: Clinical Characteristics, Treatment, and Outcomes. Clin J Am Soc Nephrol. 2007; 2:445–453. [PubMed: 17699450]
11. Elmore JG, et al. Diagnostic Concordance Among Pathologists Interpreting Breast Biopsy Specimens. Jama. 2015; 313:1122. [PubMed: 25781441]
12. Chen F, et al. Nanoscale imaging of RNA with expansion microscopy. Nat Methods. 2016; 13:679–84. [PubMed: 27376770]
13. Leproust, EM., Chen, S., Ruvolo, M. Synthesis of long fish probes. 2014. at <http://www.google.com/patents/US20140256575>
14. Schnell SA, Staines WA, Wessendorf MW. Reduction of lipofuscin-like autofluorescence in fluorescently labeled tissue. J Histochem Cytochem. 1999; 47:719–730. [PubMed: 10330448]
15. Viegas MS, Martins TC, Seco F, Do Carmo A. An improved and cost-effective methodology for the reduction of autofluorescence in direct immunofluorescence studies on formalin-fixed paraffin-embedded tissues. Eur J Histochem EJH. 2007; 51:59.
16. Neumann M, Gabel D. Simple Method for Reduction of Autofluorescence in Fluorescence Microscopy. J Histochem Cytochem. 2002; 50:437–439. [PubMed: 11850446]
17. Mendez MG, Kojima SI, Goldman RD. Vimentin induces changes in cell shape, motility, and adhesion during the epithelial to mesenchymal transition. FASEB J. 2010; 24:1838–51. [PubMed: 20097873]
18. Maier J, Traenkle B, Rothbauer U. Real-time analysis of epithelial-mesenchymal transition using fluorescent single-domain antibodies. Sci Rep. 2015; 5:13402. [PubMed: 26292717]
19. Pease DC. Fine structures of the kidney seen by electron microscopy. J Histochem Cytochem. 1955; 3:295–308. [PubMed: 13242788]
20. Ranganathan S. Pathology of Podocytopathies Causing Nephrotic Syndrome in Children. Front Pediatr. 2016; 4:32. [PubMed: 27066465]
21. Hirose T, et al. An essential role of the universal polarity protein, aPKC??, on the maintenance of podocyte slit diaphragms. PLoS One. 2009; 4
22. Dandapani SV, et al. ??-actinin-4 is required for normal podocyte adhesion. J Biol Chem. 2007; 282:467–477. [PubMed: 17082197]
23. Mundel P, et al. Synaptopodin: An actin-associated protein in telencephalic dendrites and renal podocytes. J Cell Biol. 1997; 139:193–204. [PubMed: 9314539]
24. Sim J, Wright CC. The kappa statistic in reliability studies: use, interpretation, and sample size requirements. Phys Ther. 2005; 85:257–68. [PubMed: 15733050]

25. Degnim AC, et al. Gene signature model for breast cancer risk prediction for women with sclerosing adenosis. Breast Cancer Res Treat. 2015; 152:687–694. [PubMed: 26202055]
26. Allison KH, et al. Understanding diagnostic variability in breast pathology: Lessons learned from an expert consensus review panel. Histopathology. 2014; 65:240–251. [PubMed: 24511905]
27. Dong F, et al. Computational pathology to discriminate benign from malignant intraductal proliferations of the breast. PLoS One. 2014; 9
28. Chozinski TJ, et al. Expansion microscopy with conventional antibodies and fluorescent proteins. Nat Methods. 2016; 13:1–7.
29. Ku T, et al. Multiplexed and scalable super-resolution imaging of three-dimensional protein localization in size-adjustable tissues. Nat Biotech. 2016; 34:973–981.
30. Lubeck E, Cai L. Single-cell systems biology by super-resolution imaging and combinatorial labeling. Nat Methods. 2012; 9:743–8. [PubMed: 22660740]
31. Lubeck E, Coskun AF, Zhiyentayev T, Ahmad M, Cai L. Single-cell in situ RNA profiling by sequential hybridization. Nat Methods. 2014; 11:360–361. [PubMed: 24681720]
32. Chen KH, Boettiger AN, Moffitt JR, Wang S, Zhuang X. Spatially resolved, highly multiplexed RNA profiling in single cells. Science. 2015; 348:aaa6090. [PubMed: 25858977]
33. Jungmann R, et al. Multiplexed 3D cellular super-resolution imaging with DNA-PAINT and Exchange-PAINT. Nat Methods. 2014; 11:313–8. [PubMed: 24487583]
34. Germroth PG, Gourdie RG, Thompson RP. Confocal microscopy of thick sections from acrylamide gel embedded embryos. Microsc Res Tech. 1995; 30:513–20. [PubMed: 7541260]
35. Chen F, et al. Nanoscale imaging of RNA with expansion microscopy. Nat Methods. 2016; 13:679–84. [PubMed: 27376770]
36. Irshad H, Veillard A, Roux L, Racoceanu D. Methods for nuclei detection, segmentation, and classification in digital histopathology: A review-current status and future potential. IEEE Rev Biomed Eng. 2014; 7:97–114. [PubMed: 24802905]
37. Lowe DG. Distinctive Image Features from Scale-Invariant Keypoints. Int J Comput Vis. 2004; 60:91–110.
38. Vedaldi, A., Fulkerson, B. Proceedings of the international conference on Multimedia - MM '10. ACM Press; 2010. Vlfeat; p. 1469
39. Sternberg SR. Biomedical image processing. Computer (Long Beach Calif). 1983; 16:22–34.
40. Zuiderveld K. Contrast limited adaptive histogram equalization. Graphics gems IV. 1994:474–485.
41. Fan J. Notes on Poisson distribution-based minimum error thresholding. Pattern Recognit Lett. 1998; 19:425–431.
42. Al-Kofahi Y, Lassoued W, Lee W, Roysam B. Improved automatic detection and segmentation of cell nuclei in histopathology images. IEEE Trans Biomed Eng. 2010; 57:841–52. [PubMed: 19884070]
43. Haralick RM, Shanmugam K, Dinstein I. Textural Features for Image Classification. IEEE Trans Syst Man Cybern. 1973; 3:610–621.
44. Galloway MM. Texture Analysis using Gray Level Run Lengths. Comput Graph Image Process. 4:172–179. 19675.
45. Friedman J, Hastie T, Tibshirani R. Regularization Paths for Generalized Linear Models via Coordinate Descent. J Stat Softw. 2010; 33:1–22. [PubMed: 20808728]
46. Tibshirani R. Regression shrinkage and selection via the lasso. J R Statis Soc B. 1996; 58:267–288.
47. Dormann CF, et al. Collinearity: a review of methods to deal with it and a simulation study evaluating their performance. Ecography (Cop). 2013; 36:27–46.
48. Breiman L. Random forests. Mach Learn. 2001; 45:5–32.
49. John GH, Langley P. Estimating continuous distributions in Bayesian classifiers. Proceedings of the Eleventh conference on Uncertainty in artificial intelligence. 1995:338–345.

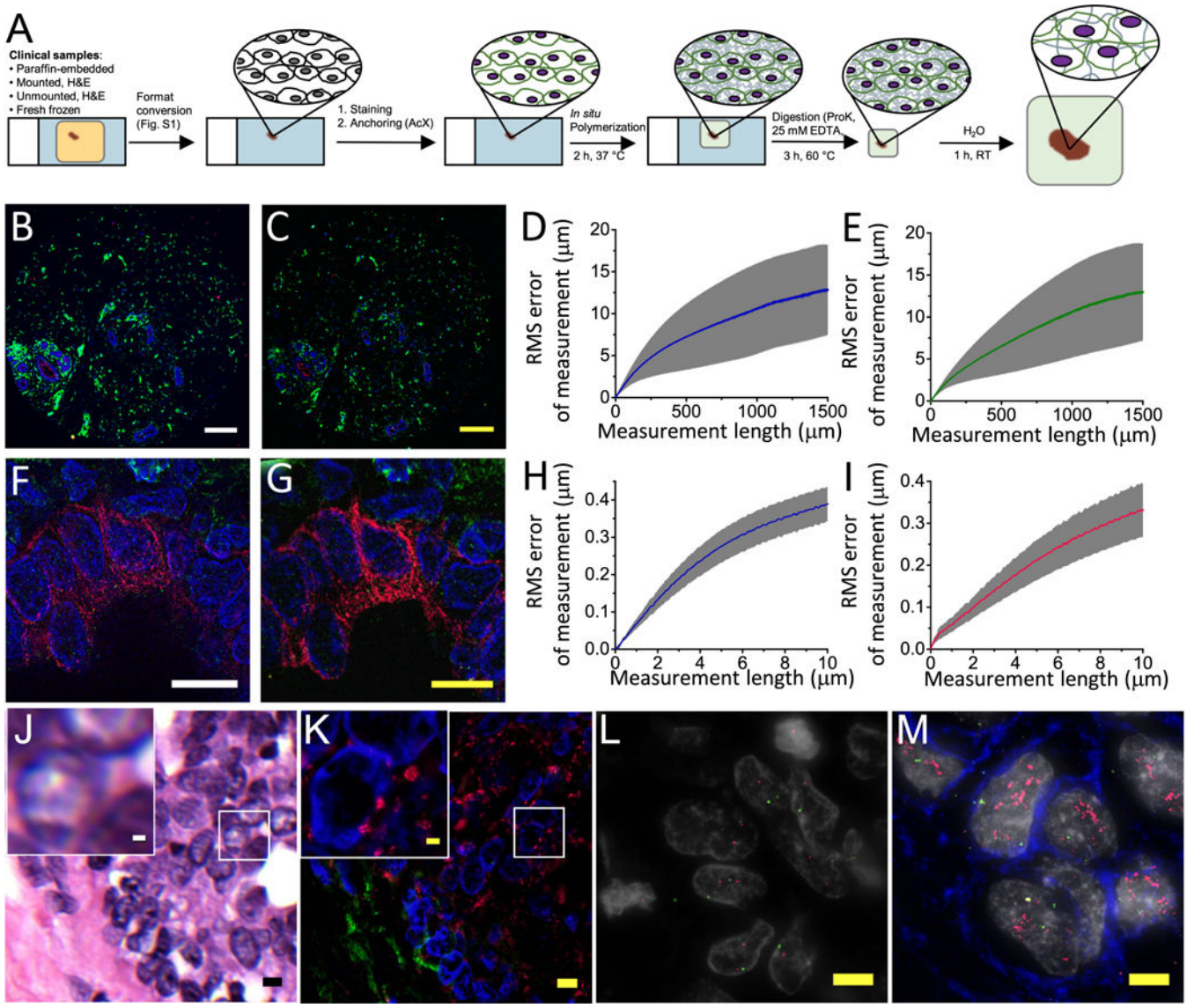

Figure 1. Design and validation of expansion pathology (ExPath) chemical processing

(**A**) Schematic of ExPath workflow (details in Supplementary Fig. 1). (**B**) Pre-expansion image of a 1.5 mm core of normal human breast tissue acquired with a widefield epifluorescent microscope. Blue, DAPI; green, vimentin; magenta, voltage-dependent anion channel (VDAC). (**C**) Post-expansion (i.e., ExPath) widefield fluorescent image of the sample of **B**. (**D** and **E**) Root mean square (RMS) length measurement error as a function of measurement length for pre- vs post-expansion images (blue solid line, mean of DAPI channel; green solid line, mean of vimentin channel; shaded area, standard error of mean; n = 3 samples from different patients. Average expansion factor: 4.3 (standard deviation (SD): 0.3)). (**F**) Super-resolution structured illumination microscopy (SR-SIM) image of normal human breast tissue. Blue, DAPI; green, vimentin; magenta, keratin-19 (KRT19). (**G**) ExPath image of the sample of **F** acquired with a spinning disk confocal microscope. (**H** and **I**) RMS length measurement error as a function of measurement length for ExPath vs SIM images of human breast tissue (blue solid line, mean of DAPI channel; magenta solid line,

mean of KRT19 channel; shaded area, standard error of mean; n = 5 fields of view from samples from 4 different patients. Average expansion factor: 4.0 (SD: 0.2)). (**J**) Hematoxylin and eosin (H&E) stained human breast sample with atypical ductal hyperplasia (ADH). Inset (upper left) is a magnified view of the area framed by the small square at right. (**K**) ExPath widefield fluorescent image of the sample of **J**, stained with antibodies against Hsp60 (magenta) and vimentin (green), and DAPI (blue). (**L**) ExPath widefield fluorescent image of a human breast cancer sample without *HER2* amplification. Blue, anti-HER2 (not visible); gray, DAPI; green, DNA FISH against chromosome 17 centrosome; magenta, DNA FISH against HER2. (**M**) ExPath widefield fluorescent image of a human breast cancer sample with *HER2* amplification, stained as in **L**. Scale bars (yellow scalebars indicate post-expansion images): (**B**) 200 μm; (**C**) 220 μm (physical size post-expansion, 900 μm; expansion factor 4.1); (**F**) 10 μm; (**G**) 10 μm (physical size post-expansion, 43 μm, expansion factor 4.3); (**J**) 5 μm, inset 1 μm; (**K**) 5 μm, inset 1 μm (physical size post-expansion, 23 μm; inset, 4.6 μm; expansion factor 4.6); (**L**) and (**M**), physical size post-expansion 20 μm.

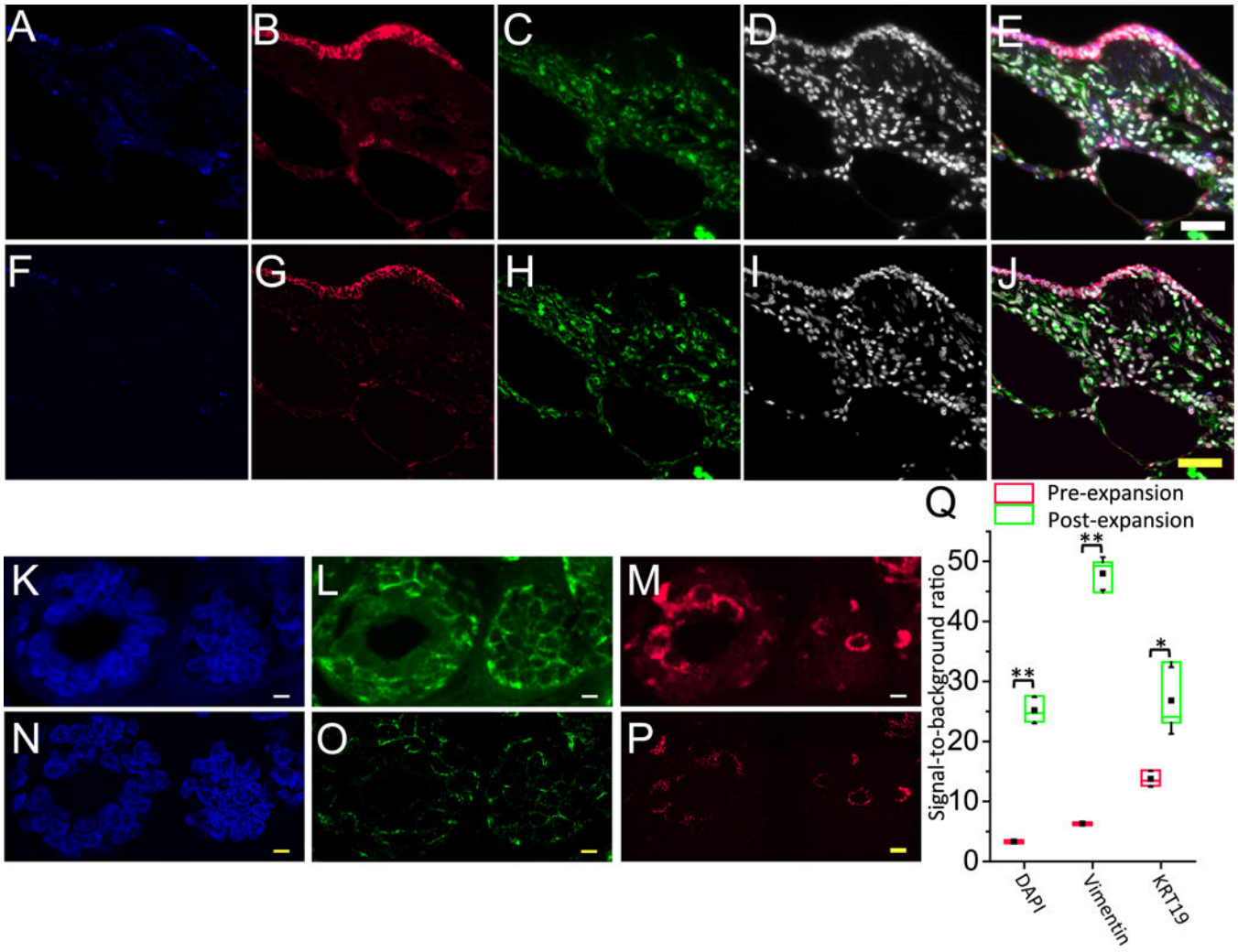

Figure 2. ExPath reduction of tissue autofluorescence

(A–J) Widefield images of normal human lung tissue, labeled with DAPI (gray) and antibodies against ACTA2 (blue), vimentin (green), and KRT19 (magenta), showing pre- **(A–E)** and post- **(F–J)** expansion data. **(K–P)** Confocal images of normal human breast tissue, labeled with DAPI (blue) and antibodies against vimentin (green) and KRT19 (magenta), showing pre- **(K–M)** and post- **(N–P)** expansion data. **(Q)** Signal-to-background ratio for pre-expansion (magenta) as well as post-expansion (green) states of n=3 samples of breast tissue from 3 patients. Average expansion factor: 4.1 (SD: 0.1). ** P<0.01, * P<0.1, two-tailed paired t-test. The ends of whiskers are defined by the SD; the upper and lower boundaries of the box are defined by the maximum and minimum, respectively; the segment in the rectangle indicates the median; the square symbol indicates the mean. Scale bars (yellow indicates post-expansion image): (**E**) 45 μm; (**J**) 45 μm (physical size post-expansion, 208 μm; expansion factor 4.6); **(K–M)** 5 μm; **(N–P)** 5 μm (physical size post-expansion, 18 μm; expansion factor 4.0).

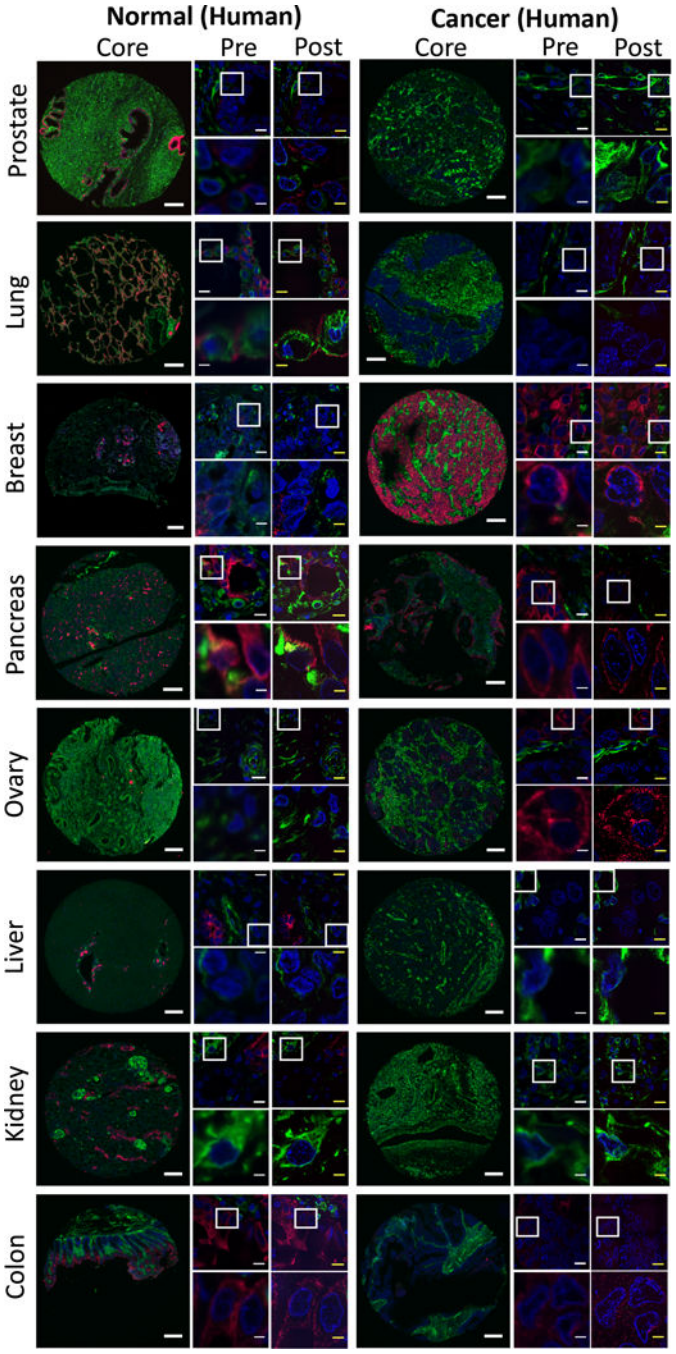

Figure 3. ExPath imaging of a wide range of human tissue types

Images of various tissue types for both normal (left images) and cancerous (right images) tissues from human patients. From top to bottom, different rows show different tissue types as labeled (e.g., prostate, lung, breast, etc.). Within each block of images for a given tissue × disease type, there are 5 images shown. The leftmost of the 5 images shows a core from a tissue microarray (scale bar, 200 μm). The middle column within the 5 images shows two images, the top of which is a small field of view (scale bar, 10 μm), and the bottom of which zooms into the area outlined in the top image by a white box (scale bar, 2.5 μm). The right

column within the 5 images shows the same fields of view as in the middle column, but post-expansion (yellow scale bars;top images, 10 – 12.5 μm; bottom images, 2.5 – 3.1 μm; physical size post-expansion, top images, 50 μm; bottom images, 12.5 μm; expansion factors 4.0–5.0x, see Supplementary Table 3 for raw data). Blue, DAPI; green, vimentin; magenta, KRT19.

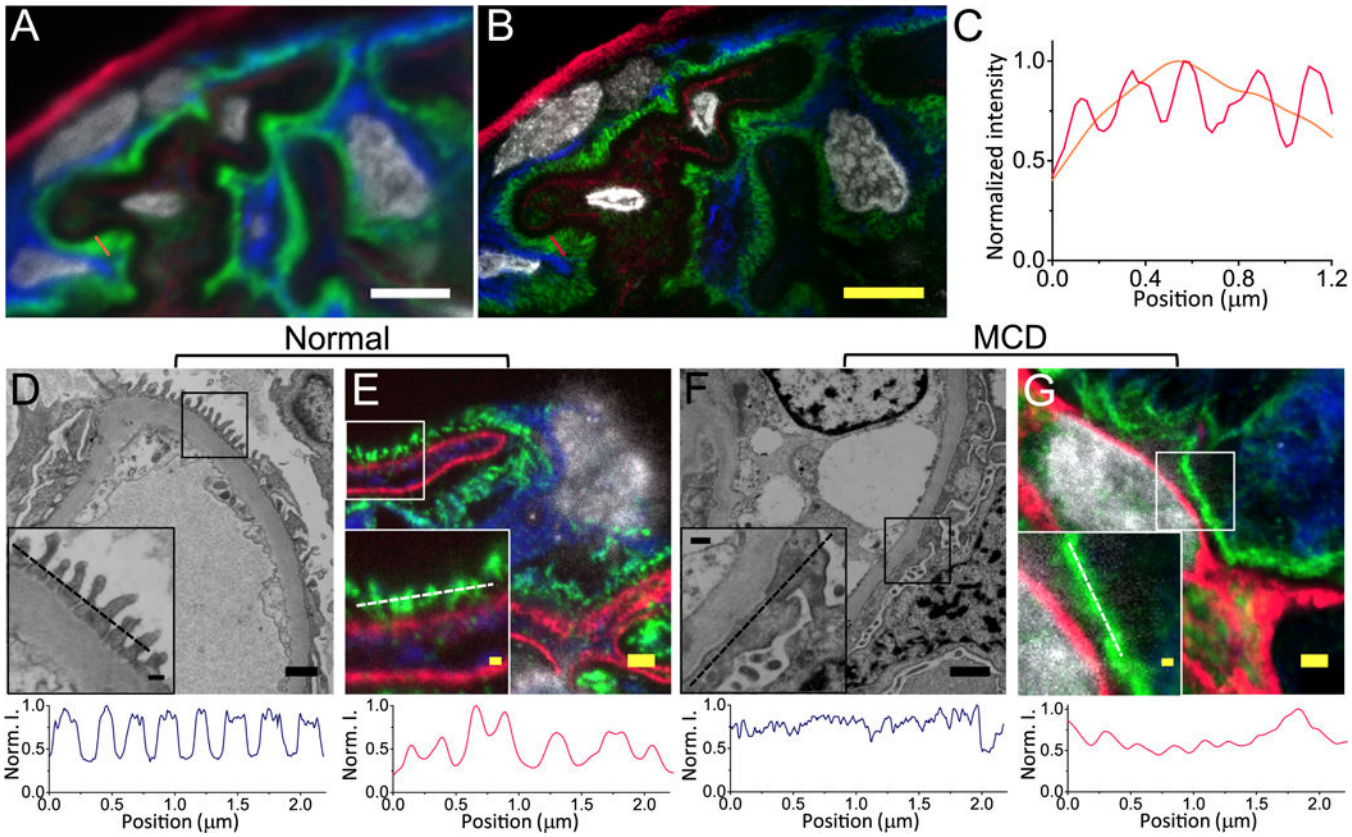

Figure 4. ExPath analysis of kidney podocyte foot process effacement

(**A**) Pre-expansion confocal image of a normal human kidney sample showing part of a glomerulus acquired with a spinning disk confocal microscope. Blue, vimentin; green, actinin-4; magenta, collagen IV; grey, DAPI. Orange dotted line indicates the line cut analyzed in **C**. (**B**) ExPath image of the sample of **A**, using the same microscope. Magenta dotted line indicates the line cut analyzed in **C**. (**C**) Profiles of actinin-4 intensity along the orange and magenta dotted lines of (**A**) and (**B**). (**D**) Electron micrograph of a clinical biopsy sample from a normal human kidney. Inset, zoom into the region outlined by the black box; dotted line within the inset indicates the line cut analyzed in the graph below the image. Below, electron micrograph feature intensity along the line cut of the inset, normalized to maximum intensity ("Norm. I."). (**E**) ExPath image of a clinical kidney biopsy sample from the same patient analyzed in (**D**), stained as in (**A**). Inset, zoom into the region outlined by the white box; dotted line within the inset indicates the line cut analyzed below. Below, actinin-4 intensity along the line cut of the inset, normalized as in **D**. (**F**) As in **D**, but for a patient with minimal change disease (MCD). (**G**) As in **E**, but for the same patient as in **F**. Scale bars (yellow indicates a post-expansion image): (**A**) 5 μm; (**B**) 5 μm (physical size post-expansion, 23.5 μm; expansion factor: 4.7); (**D**) 1 μm; inset, 200 nm; (**E**) 1 μm (physical size post-expansion, 4.3 μm; expansion factor: 4.3); inset, 200 nm; (**F**) 1 μm, inset, 200 nm; (**G**) 1 μm (physical size post-expansion, 4.2 μm; expansion factor: 4.2); inset, 200 nm.

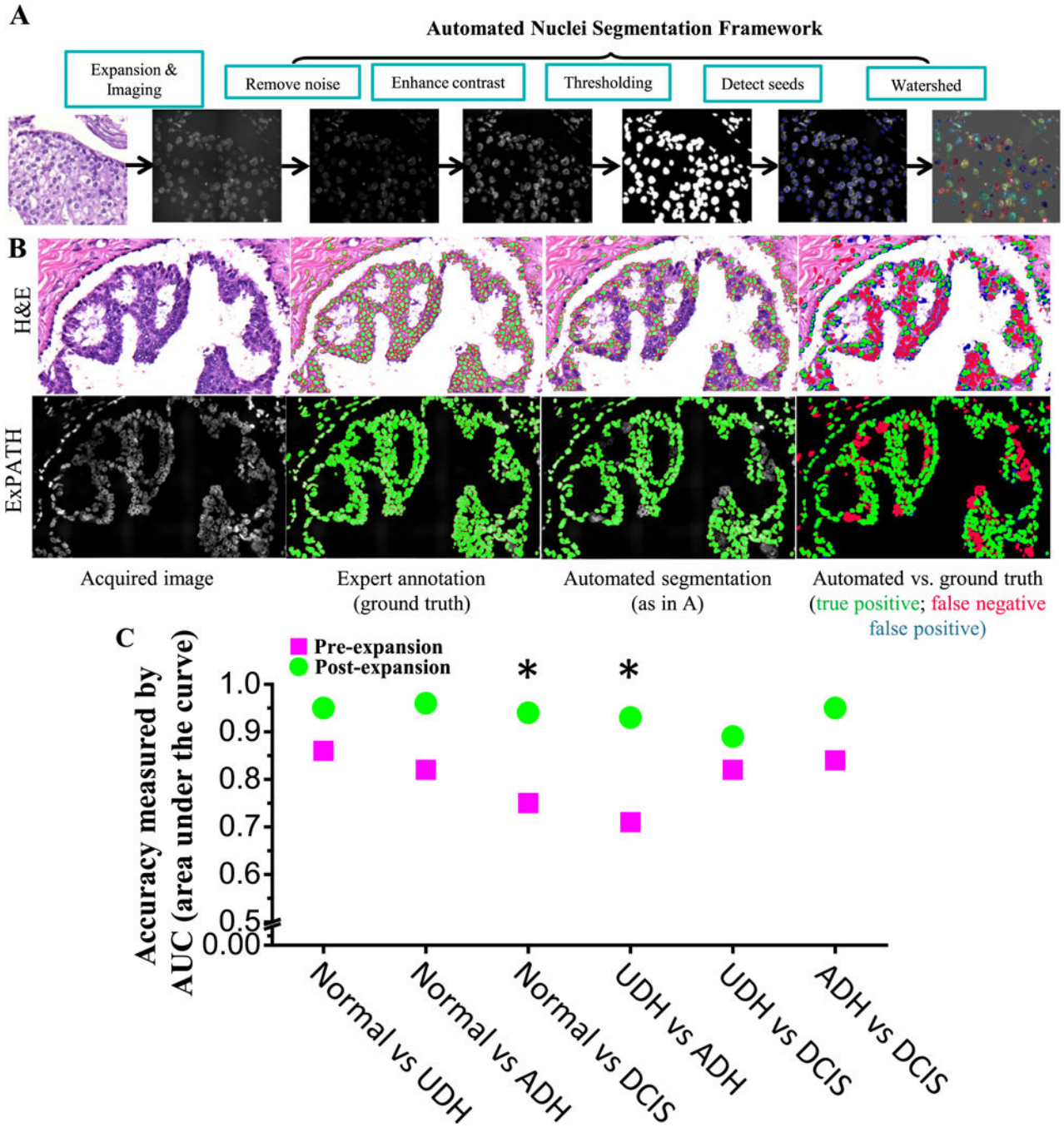

Figure 5. ExPath improvement of computational diagnosis of early breast lesions

(**A**) Automated nucleus segmentation framework, showing steps of the image pre-processing and nuclei segmentation pipeline. From left to right: noise removal using rolling ball correction, enhancing contrast by histogram equalization, nucleus segmentation by minimum error thresholding, seed detection by multi-scale Laplacian of Gaussian (LoG) filter, nuclei splitting by marker-controlled watershed. (**B**) Computational detection and segmentation of nuclei is significantly more accurate in expanded samples vs. pre-expanded samples: example of atypical ductal hyperplasia (ADH). For the “expert annotation” and

"automated segmentation" columns: green filled nuclei are nuclei segmented by the expert or the automated segmentation algorithm, respectively (red circles indicate nucleus outlines, which are not visible in the ExPath row because the resolution is too high and thus the outline is barely visible). In the "automated vs expert" column: green filled nuclei, true positives; red filled nuclei, false negatives; blue filled nuclei, false positives (note that when the automated segmentation yielded larger outlines than the expert, this is expressed as a blue "halo" around the green). (**C**) Classification models were built using L1-regularized logistic regression (the GLMNET classifier). Classification accuracy was measured as the area under the receiver operator curve (AUC) achieved by the classification model in cross-validation. We applied this image classification framework on both pre-expanded H&E and post-expanded DAPI images for computational differentiation of normal, benign and pre-invasive malignant breast diseases. Both data sets consisted of 105 images, containing 36 normal breast tissue images, 31 benign breast tissue images (15 UDH and 16 ADH) and 38 non-invasive breast cancer tissue images (DCIS). Average expansion factor: 4.8 (SD: 0.3). * $P<0.05$, bootstrapped paired t-test. *P* value for each binary comparison: Normal vs. UDH (0.17); Normal vs. ADH (0.34); Normal vs. DCIS (0.24); UDH vs. ADH (0.02); UDH vs. DCIS (0.01); ADH vs. DCIS (0.24).